Observation of Valence Band Crossing: The Thermoelectric Properties of CaZn2Sb2-CaMg2Sb2 Solid Solution

Journal:	*Journal of Materials Chemistry A*
Manuscript ID	TA-ART-03-2018-002250.R1
Article Type:	Paper
Date Submitted by the Author:	04-Apr-2018
Complete List of Authors:	Wood, Max; Northwestern University, Materials Science and Engineering Aydemir, Umut; Koc Universitesi Fen Fakultesi, Chemistry Ohno, Saneyuki; California Institute of Technology, Materials Science Snyder, G. Jeffrey; Northwestern University, Materials Science

Journal Name

ARTICLE

Observation of Valence Band Crossing: The Thermoelectric Properties of $CaZn_2Sb_2$-$CaMg_2Sb_2$ solid solution

`Received 00th January 20xx,
Accepted 00th January 20xx

DOI: 10.1039/x0xx00000x

www.rsc.org/

Max Wood[a], Umut Aydemir[a,b*], Saneyuki Ohno[a,c,d], and G. Jeffrey Snyder [a*]

$CaAl_2Si_2$ type Zintl phases have long been known to be promising thermoelectric materials. Here we report for the first time on the thermoelectric properties of $CaMg_2Sb_2$ along with the transport properties of $CaZn_2Sb_2$-$CaMg_2Sb_2$ solid solution. The charge carrier tuning in this system was carried out by substituting divalent Ca^{2+} with monovalent Na^+. To check a possible band convergence, we applied an effective mass analysis to our samples and found an abrupt doubling of the samples' effective masses as the composition switches from Zn-rich to Mg-rich. We further analyzed the effect that alloy scattering plays in the lattice thermal conductivity of our samples with a Modified Klemens model. We showed that the reduction seen in the lattice thermal conductivity of the alloyed samples can be well explained based on the mass difference of Mg and Zn in the poly-anionic metal site. Our best p-doped sample with a composition of $Ca_{.99}Na_{.01}MgZnSb_2$ displays relatively high peak *zT* of 0.87 at 850K.

Introduction

Creating a sustainable renewable energy future relies on diversifying our current energy resources (solar, wind, geothermal, etc.) and a reduction in overall energy consumption. In 2016 over half of all energy used in the United States was lost to waste heat, and if even a small portion of this energy was recaptured it could transform the energy landscape[1]. Thermoelectric materials are a category of materials that can interconvert gradients in electrical potential and temperature, which allows for waste heat to be harvested into usable energy. Thermoelectric devices are scalable and have no moving parts making them incredibly reliable and suited for some niche applications where traditional heat engines could not be employed.

The efficiency of thermoelectric generators, like all heat engines, are limited by the Carnot efficiency ($\eta_{max} = \frac{\Delta T}{T_{hot}} \frac{\sqrt{1+zT}-1}{\sqrt{1+zT}+1}$). Here *zT* is material's thermoelectric figure of merit defined as $zT = \frac{\alpha^2 T}{\rho\kappa}$, where α is Seebeck coefficient, ρ is resistivity, T is temperature, and κ is thermal conductivity. Optimizing a material's efficiency has proven challenging due to the conflicting and intertwined nature of these transport properties. In order to maximize *zT* a material must have a high Seebeck coefficient, (found in low carrier concentration insulators), and a low resistivity (found in high carrier concentration metals)[2]. One way of maximizing both Seebeck coefficient and conductivity is by looking for materials with high valley degeneracy [3-6]. Increasing the number of valleys present increases a materials Seebeck coefficient while minimally impacting the carrier's mobility. [3, 7, 8]

The material's thermal conductivity, which is desired to be low, can be broken into its electronic and lattice parts given by $\kappa = \kappa_e + \kappa_l$. The electronic portion is directly tied to the materials conductivity given by $\kappa_e = L\sigma T$ where L is the materials Lorenz number, however the lattice portion of the thermal conductivity isn't directly related to carrier concentration. Avenues of decreasing κ_l such as increasing the complexity and size of the unit cell [9], changing the materials microstructure to scatter phonons [10-13], and alloying the material to scatter phonons [14-16] have been shown to work well.

Zintl phases constitute large group of materials many of which ($Yb_{14}MnSb_{11}$ [17], $Ca_3Al_3Sb_3$ [18] $Ca_9Zn_4Sb_9$, [19] $BaGa_2Sb_2$ [20], Mg_3Sb_2 [21], *etc.*) are known for having high thermoelectric efficiencies. These phases are made up of an electropositive metal (alkali, alkali earth or rare-earth) that donates its electrons to an anionic substructure forming covalent bonds. This unique way of bonding often leads to very complex and sometimes large crystal structures leading inherently low lattice thermal conductivities.[2]

P-type 1-2-2 Zintls have been shown to display high thermoelectric efficiencies [22-32]. $CaZn_2Sb_2$ and $CaMg_2Sb_2$ both have the $CaAl_2Si_2$ structure type ($P\bar{3}m1$) (Fig. 1). Having isotypic crystal structure, these compounds very easily form solid solutions with one another. The structure can be described as having two-atom thick layers of

---

[a] *Department of Materials Science and Engineering, Northwestern University, Evanston, Illinois 60208, United States*
[b] *Department of Chemistry, Koc University, Sariyer, Istanbul-34450, Turkey*
[c] *Department of Applied Physics and Materials Science, California Institute of Technology, Pasadena, California 91125, USA*
[d] *Institute of Physical Chemistry, Justus-Liebig-University Giessen, Heinrich-Buff-Ring 17, D-35392 Giessen, Germany*
** Author for correspondence; email: uaydemir@ku.edu.tr, jeff.snyder@northwestern.edu.*

Electronic Supplementary Information (ESI) available: [details of any supplementary information available should be included here]. See DOI: 10.1039/x0xx00000x an ionic substructure of $(Zn_{2-x}Mg_xSb_2)^{-2}$, where each Sb and Zn(Mg) atom is four-fold coordinated. Ca atoms separate these layers and are located in the octahedral interstices formed by Sb atoms [33].

Zhang et al. largely inspired this work where they laid out an approach to create valley degeneracy in a material by converging the energies of the p_x, p_y, and p_z valence band maximum in compounds of the $CaAl_2Si_2$ structure [34]. These different bands may each have a different mobility and effective mass that will affect transport in the material [35]. In $CaMg_2Sb_2$ the p_z band is above the p_x and p_y bands by approximately 0.13 eV, while in $CaZn_2Sb_2$ the p_x and p_y bands are above the p_z band by approximately 0.1 eV. Assuming linearly changing rigid bands and an inverse lever law relationship, we determined convergence would occur around the composition $CaMg_{.86}Zn_{1.14}Sb_2$ (Fig.2) . Analyzing transport using a single parabolic band type model, we would expect the DOS effective mass of the converged sample to peak at a local maximum according to $(m_{DOS}^*)^{\frac{3}{2}} = N_V(m_b)^{3/2}$, with the masses of the samples on the zinc rich side of this sample decreasing to one value, and another value for samples on the magnesium rich side [8].

These offsets and band positions can change, and even flip, depending upon the calculation [26, 34, 36]. More specifically Zhang et al. reports $CaMg_2Sb_2$ to have a singly degenerate band with a higher energy than a doubly degenerate band at Gamma at the valence band maximum[34]. Meanwhile Singh et al. reports $CaMg_2Sb_2$ to have a doubly degenerate band with a higher energy than a singly degenerate band at Gamma at the valence band maximum[36]. Furthermore a sample's physical properties measured at elevated temperatures may differ from DFT calculations run effectively at 0 K due to thermal expansion and phonons [37]. Therefore in addition to this predicted converged sample, samples of the end members and various compositions in between the solid solution were also synthesized and studied.

In this paper we analyze our data using an effective mass model [8, 38] and show that while we don't see a peak in effective mass, which would indicate converging bands, we do see an abrupt change, doubling the effective mass near the predicted composition. This indicates transport is changing from one set of band(s) on the Zn side to another on the Mg side. Additionally we analyze the thermal conductivity of our samples with a modified Klemens model used by Yang et al. [14] and show samples are getting a boost in *zT* due to alloy scattering in the lattice thermal conductivity. Furthermore we report the thermoelectric properties of $CaMg_2Sb_2$ for the first time and obtain a peak *zT* of 0.87 in the sample $Ca_{.99}Na_{.01}MgZnSb_2$ at 850 K.

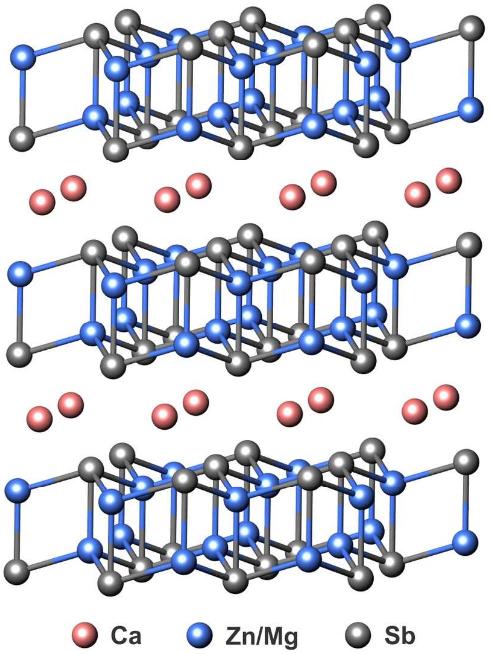

Figure 1. Crystal structure of $CaZn_{2-x}Mg_xSb_2$ with layers of anionic $(Zn_{2-x}Mg_xSb_2)^{-2}$ separated by Ca^{2+} cations.

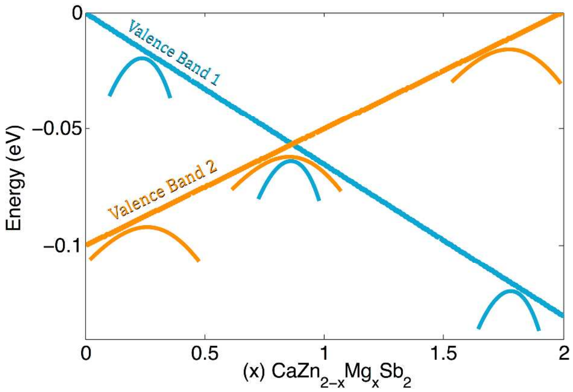

Figure 2. Visualization of the predicted energy offsets of the valence bands in the $CaZn_2Sb_2$-$CaMg_2Sb_2$ solid solution. Offsets in the end members were taken from Zhang et al. [34] and then linearly interpolated with changing composition.

Experimental Methods

Sample Preparation

Samples of Ca$_{1-y}$Na$_y$ Zn$_{2-x}$Mg$_x$Sb$_2$ (x = 0, .25, .5, .86, 1, 1.5,2) (y = 0, .01) were prepared via a high-energy ball mill using stoichiometric ratios of bulk Ca dendrites (99.99% Sigma-Aldrich), Zn shot (99.999% Alpha Aesar), annealed Mg slugs (99.95% Alpha Aesar), Sb shot (99.999% Alpha Aesar), and Na sticks (99% Alpha Aesar). Starting elements were cut into small pieces and loaded into a steel ball-milling vial with two ½ inch and four ¼ inch stainless steel balls. All samples were milled using a SPEX Sample Prep 800 Series Mixer/Mill for 3 90-minute periods in between which the contents of the vial were scraped in an inert atmosphere in order to ensure elements were reacting homogenously. Samples were consolidated using an induction heated rapid hot-press [39] under a flowing argon atmosphere within a ½ in diameter high-density graphite die (POCO) into pellets approximately 2 mm in thickness. Samples were pressed at 350 °C for 30 minutes to ensure any elemental zinc was fully reacted and then 700°C for 90 minutes at a pressure of 45 MPa. Resulting Samples were found to have densities exceeding 95%. All Samples are metallically shiny and relatively stable under ambient conditions.

Sample Characterization

XRD was performed on polished pellets using a Rigaku Dmax Powder X-Ray Diffractometer (45kV, 40 mA, Cu Kα radiation) with reflection geometry. Density of the samples was measured using the Archimedes' principle. Electronic transport measurements were measured under dynamic high vacuum up to 875 K with a ramp speed of 75 K/h. Resistivity and hall coefficients were measured concurrently using the Van Der Pauw technique with pressure-assisted molybdenum contacts equipped a 2 T magnet[40]. Thermal diffusivity measurements were taken with a Netzch LFA 457 under purged flowing argon up to 875K with a ramp speed of 75 K/h. Thermal conductivity was calculated estimating heat capacity with the Dulong-Petit law. Seebeck coefficients were measured under dynamic high vacuum up to 875 K with a homebuilt system using Chromel-Nb thermocouples [41]. All Samples were investigated in pellet form with Seebeck and thermal diffusivity being measured out of plane and resistivity and Hall coefficient being measured in plane direction. From the analysis of X-ray diffraction data, there appears to be no form of texturing or preferred orientation after pressing.

Results and Discussion

X-Ray Diffraction

X-ray diffraction shows a solid solution was indeed obtained for all compositions tried with the lattice parameters linearly increasing as Mg substitutes Zn on the transition metal site (Fig. 3). X-ray analysis further reveals there is no substantial impurity phase in our samples (See Figure S1 in SI).

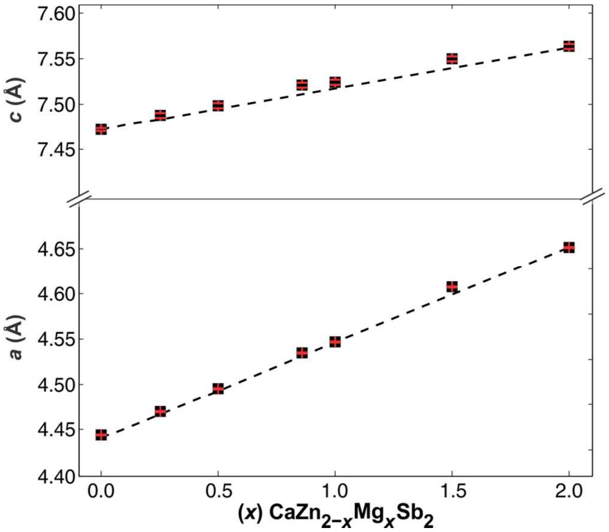

Figure 3. Lattice parameters a and c for compounds CaZn$_{2-x}$Mg$_x$Sb$_2$ (x = 0, .25, .5, .86, 1, 1.5, 2) determined from x-ray diffraction analysis. The error is shown in red, and the dashed line is a guide to the eye. Note that the error in all samples is less than the point side of the data.

Results

From previous DFT studies we expect the band gap to widen as we substitute Mg on to the Zn site [36] [22]. Samples without Na doping decrease in carrier concentration as Mg^{2+} substitutes Zn^{2+} widening the band gap and changing the sample from degenerately doped p-type at the Zn side to an intrinsic insulator on the Mg side (See Figure S3 & S4 in SI). Seebeck coefficient and resistivity follow a similar trend; both increasing with the substitution of Mg for Zn.

Samples with nominal composition CaZn$_{.5}$Mg$_{1.5}$Sb$_2$ and CaMg$_2$Sb$_2$ were too resistive to measure in our hall measurement system. Therefore Na was chosen as a p-dopant for samples whose carrier concentrations were less than optimal, because of its similar ionic radii to Calcium (See Figure S4 in SI). Samples with nominal compositions Ca$_{0.99}$Na$_{0.01}$Zn$_{2-x}$Mg$_x$Sb$_2$ were then created to degenerately dope all samples (Fig. 4 & S5) in which an effective mass model [8 , 38] indicated doping was less than optimal.

Substituting Mg on to the Zn site has the effect of lowering the mobility of samples (Fig. 5). Displaying the temperature dependence of $T^{-3/2}$, the mobility data on the Zn rich-side of the solid solution is characteristic of deformation potential scattering. Moving to the Mg-rich side it appears some other type of scattering dominates at low temperatures but deformation potential scattering is still effective at higher temperatures. This low temperature behavior is likely due to grain boundary scattering seen in the related compound Mg$_3$Sb$_2$[42]. We attribute U shaped curve in sample $Ca_{.99}Na_{.01}Mg_2Sb_2$ to grain boundary scattering, with the decrease in resistivity at higher temperatures likely due to bipolar conductivity.

The thermal conductivity of the two end member samples shows an expected higher thermal conductivity than samples that are solid solutions, primarily due to alloy scattering in the solid solution samples. Samples that are doped with Na show higher thermal conductivity than their un-doped counterparts due to the electronic portion of the thermal conductivity being larger.

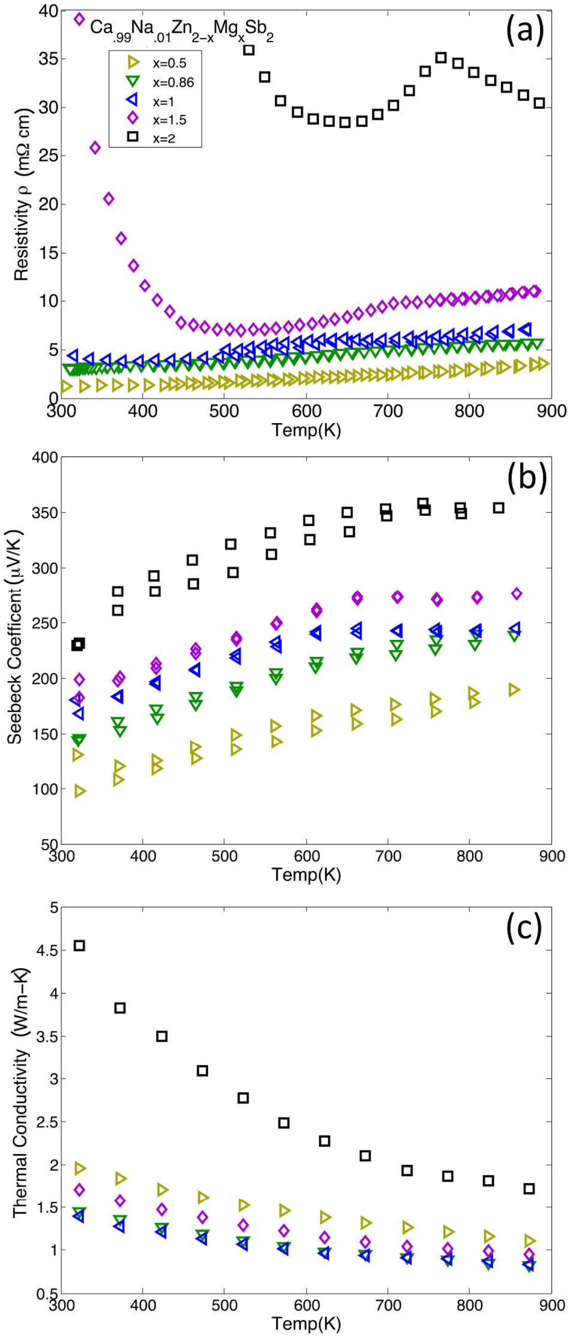

Figure 4. (a) Resistivity , (b) Seebeck, and (c) thermal conductivity data for samples with 1% nominal Na substitution on the Ca site

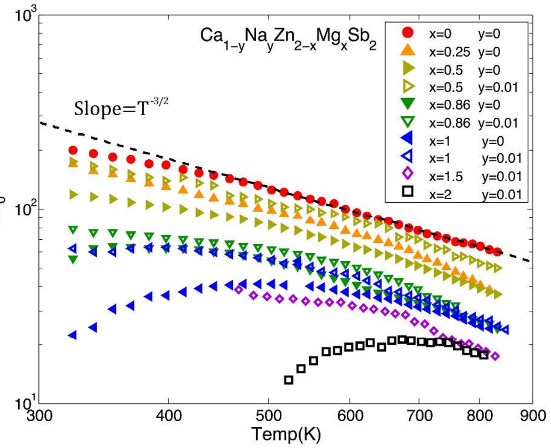

Figure 5. Mobility vs temperature for all samples measured. The addition of Mg onto the Zn site has the effect of decreasing mobility as well as changing its temperature dependence. At higher temperatures most samples have a temperature dependent mobility characteristic of deformation potential scattering.

Discussion

Effective Mass Model Analysis

To analyze and compare the electronic properties of this data set we use an effective mass model (sometimes referred to as a single parabolic band model) at 600 K [8]. This temperature was chosen to compare data because it is before the onset of bipolar conduction for most samples, indicated by a flat carrier concentration and increasing Seebeck value with temperature. Furthermore at 600 K most samples have a mobility that has a temperature dependence indicating deformation potential scattering allowing us to analyze all our data in a similar fashion (Fig. 5). We should note grain boundary scattering does not significantly affect a materials Seebeck, or hall coefficient. Therefore it is reasonable to extract a DOS effective mass from Mg rich samples using deformation potential scattering, even if the mobility's temperature dependence varies from $T^{-3/2}$.

In this system we expect Zn rich samples to have conduction from one band(s), and Mg rich samples get transport from a different band(s). At some intermediate composition we expect the bands to cross creating a converged sample with transport from both sets of bands. Modeling this converged sample's bands as a single parabolic band would give an effective mass larger than non-converged samples that are more magnesium or zinc rich. While we do not see a local maximum in effective mass for a particular composition, such as in Bi_2Te_3/Sb_2Te_3 [43] , our analysis does show effective mass acting as a step function with the Mg side having an effective mass roughly double the Zn side (Fig. 6). This indicates that transport is indeed changing from one set of bands to another.

Figure 7 shows mobility vs magnesium content for all samples at 600K. In this figure we have adjusted the data point for $Ca_{.99}Na_{.01}Mg_2Sb_2$ in an attempt to compare all samples in a regime where grain boundary scattering does not dominate conduction. This was done by scaling the mobility data of $Ca_{.99}Na_{.01}Mg_2Sb_2$ at 750K by $(750K/600K)^{3/2}$ to estimate what the mobility would be at 600K if instead deformation potential scattering were to dominate. The trend in mobility can be described using a combination of alloy and deformation potential scattering[42]. The trends can be qualitatively explained using a single deformation potential $\Xi = 10\,eV$ and the same scattering potential U = 0.5 eV for both the Zn-rich and Mg-rich samples – if one assumes the bands of the Mg-rich material is doubly degenerate and the Zn-rich is a single band .

Lattice thermal conductivity does benefit from the solid solution with compositions close to half the Zn sites filled with Mg having the lowest thermal conductivity resulting in a unitless quality factor [38 8]:

$$B = \frac{k_B^2}{e}\frac{(2m_e k_B)^{\frac{3}{2}}}{3\pi^2\hbar^3}\frac{\mu_0\left(\frac{m_S^*}{m_e}\right)^{\frac{3}{2}}T^{\frac{5}{2}}}{\kappa_L} \qquad \text{(eq 1)}$$

that peaks around these compositions (Fig. 8). Quality factor is a material metric that is independent of reduced chemical potential and therefore should be the same for samples of the same composition with different carrier concentrations. However our data shows that undoped samples with composition $CaZn_{1.14}Mg_{.86}Sb_2$ and $CaZn_{1.5}Mg_{.5}Sb_2$ have much lower quality factors than their doped counterparts. This is due to the weighted mobilities of these samples being different from their undoped counterparts.

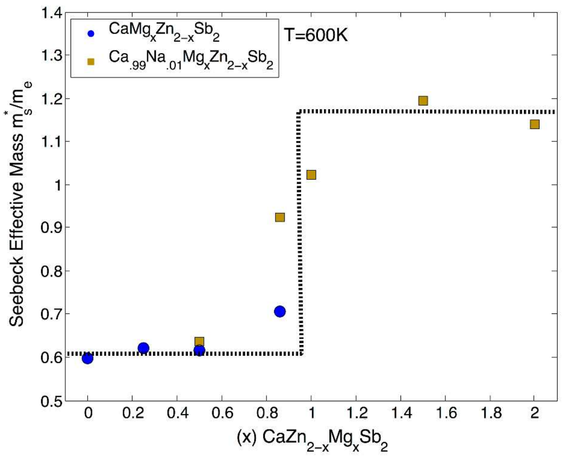

Figure 6. Seebeck effective mass [35] vs Mg content of samples at 600 K. While we do not see a maximum indicating band convergence, we do see a step function around the composition we expected convergence to appear indicating that transport is changing from one set of bands to another. The dashed line is a guide for the eye.

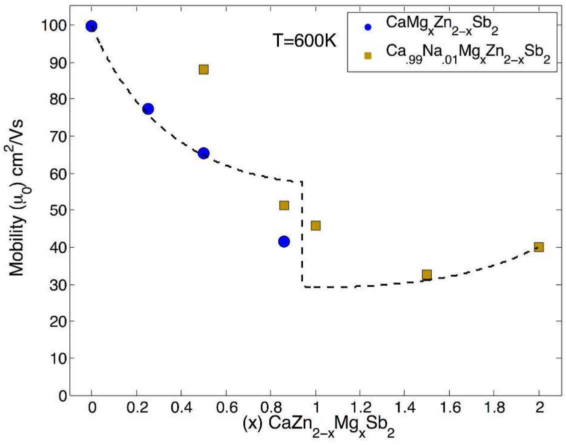

Figure 7. Mobility vs Mg content of different samples at 600 K. The data for $Ca_{.99}Na_{.01}Mg_2Sb_2$ was taken at 750K then adjusted back to 600K assuming only acoustic phonon scattering· The dashed line is a guide for the eye. The decrease in mobility is most likely due to alloy scattering.

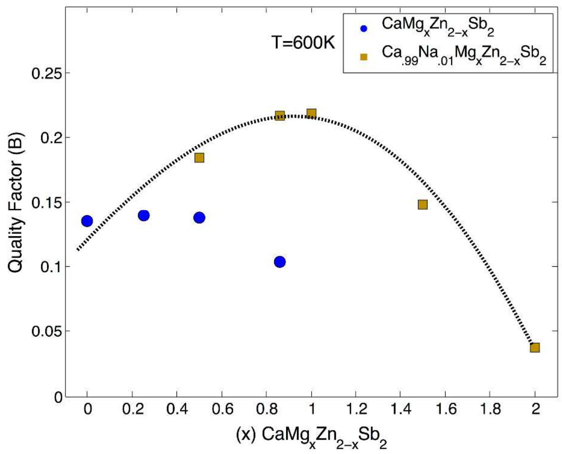

Figure 8. Quality factor vs Mg content of different samples at 600 K. Samples near the middle point of the solid solution get a boost in quality factor which is due to alloy scattering in the lattice thermal conductivity. The dashed line is a guide for the eye.

Table 1: A comparison between the solid solutions end member's thermoelectric properties at 600K. Note how the larger effective mass and grain boundary scattering in the Mg containing compound hamper mobility. Furthermore zinc's atomic mass being double that of magnesium lowers the thermal conductivity, and overall helps boost the material's quality factor (B).

	$CaZn_2Sb_2$	$Ca_{.99}Na_{.01}Mg_2Sb_2$
$m_S{}^*\ [m_e]$	0.6	1.1
$\mu_0 \left[\frac{cm^2}{Vs}\right]$	100	19
$\mu_o \left(\frac{m_S{}^*}{m_e}\right)^{\frac{3}{2}} \left[\frac{cm^2}{Vs}\right]$	45	23
$\kappa_L \left[\frac{W}{mK}\right]$	1.3	2.4
B	0.135	0.037

Lattice Thermal Conductivity Modeling

To analyze the lattice thermal conductivities we use a model described by Yang et al. [14] based on the theory of Klemens and Calloway [44-47]. This model proposes a relationship between the lattice thermal conductivities of an alloyed sample $(\kappa_{L,alloy})$ and of a pure compound used in that alloy $(\kappa_{L,pure})$ when Umklapp and point-defect scattering are dominant.

$$\frac{\kappa_{L,alloy}}{\kappa_{L,pure}} = \frac{\tan^{-1}(u)}{u} \quad \text{(eq.2)}$$

$$u^2 = \frac{\pi^2 \theta_D \Omega}{h v^2} \kappa_{L,pure} \Gamma_{expt} \quad \text{(eq.3)}$$

where u is a scaling parameter, θ_D is the Debye temperature, Ω is the average atomic volume per atom, h is Planck's constant, v is the average speed of sound given by a weighted harmonic mean of the longitudinal and transverse speeds of sound, and Γ_{expt} is the experimental disorder scaling parameter. The experimental scaling parameter can be calculated by summing its mass Γ_M and strain Γ_S contributions. In this work, we assume the strain fluctuations are negligible compared to the mass difference of Mg and Zn. The mass disorder scaling parameter is given by weighted summation over all sub-lattice sites in the primitive unit cell:

$$\Gamma_M = \frac{\sum_{i=1}^{n} c_i \left(\frac{\overline{M}_i}{\overline{\overline{M}}}\right)^2 f_i^{k1} f_i^{k2} \left(\frac{M_i^1 - M_i^2}{\overline{M}_i}\right)^2}{\left(\sum_{i=1}^{n} c_i\right)} \quad \text{(eq.4)}$$

where M represents mass, i is the indexed sub-lattice site, c_i is the relative degeneracy of the sub-lattice c, f_i^k is the occupational filling fraction of sub-lattice site i of atom type "k", $\overline{M}_i$ represents the average mass atomic mass of an atom on site i and is given by $\overline{M}_i = \sum_k f_i^k M_i^k$, $\overline{\overline{M}}$ is the average atomic mass of all atoms in the compound and is given by $\overline{\overline{M}} = \frac{\sum_{i=1}^{n} c_i \overline{M}_i}{\left(\sum_{i=1}^{n} c_i\right)}$.

In this study, since the metal atoms (Zn or Mg) tetrahedrally bonded to the anion constitutes most of the disorder, these formulas simplify as follows:

$$\overline{\overline{M}} = \tfrac{1}{5}\left[M_1^{Ca} + 2 \times M_2^{Zn}(1-x) + 2 \times M_2^{Mg}(x) + 2 \times M_3^{Sb}\right]$$

$$\Gamma_M = \frac{1}{5}\left[0 + c_2 \left(\frac{\overline{M}_2}{\overline{\overline{M}}}\right)^2 f_2^{Zn} f_2^{Mg} \left(\frac{M_2^{Zn} - M_2^{Mg}}{\overline{M}_2}\right)^2 + 0\right]$$

$$\Gamma_M = \frac{1}{5}\left[2x(1-x)\left(\frac{M_2^{Zn} - M_2^{Mg}}{\overline{\overline{M}}}\right)^2\right]$$

Where x is the occupational fraction of Mg on the transition metal site. Therefore with only inputs of lattice thermal conductivity and speeds sound of the two end members compounds, the lattice thermal conductivities of alloy compositions given between can be predicted (Fig. 9). The Debye temperature was calculated using the speed of sound by $\theta_D = \frac{h v_m}{k}$, where the Debye frequency is given by $v_m = \left(\frac{3\delta}{4\pi}\right)^{1/3} v_s$, h is Plank's constant, k is Boltzmann's constant, δ is number density of atoms, and v_s is the average speed of sound.

Table 2: Speeds of sound for $CaZn_2Sb_2$ and $CaMg_2Sb$

	$\mathbf{v_T}$ (m/s)	$\mathbf{v_L}$ (m/s)	$\mathbf{v_S}$ (m/s)
$CaZn_2Sb_2$	2094	3903	2476
$CaMg_2Sb_2$	2716	4330	3101

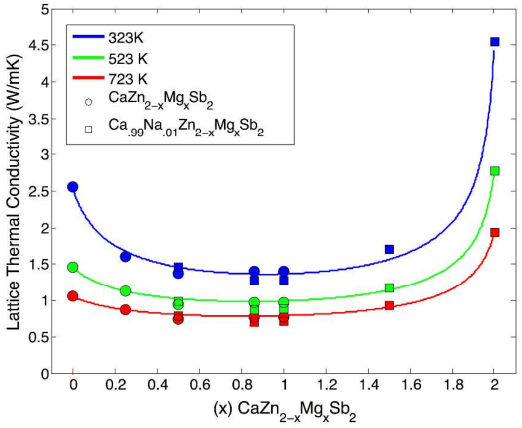

Figure 9. Lattice thermal conductivity vs Mg content. This shows a model based on simply the mass difference of the metals in the polyanionic layers can very accurately explain lattice thermal conductivity. Circles represent samples with nominal composition $CaZn_{2-x}Mg_xSb_2$. Squares represent samples with nominal composition $Ca_{.99}Na_{0.01}Zn_{2-x}Mg_xSb_2$.

Thermoelectric Performance

Fig. 10. shows the *zT* values of all the samples with respect to temperature. The samples with compositions of $Ca_{.99}Na_{.01}Zn_{1.14}Mg_{.86}Sb_2$ and $Ca_{.99}Na_{.01}ZnMgSb_2$ have the highest quality factors of all samples produced and correspondingly display the highest *zT* values. Using an effective mass model indicated that both samples were already optimally doped. (See Fig. S6 in SI).

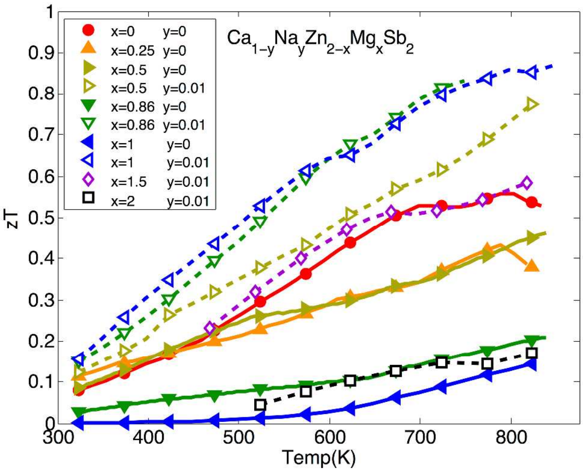

Figure 10. Thermoelectric figure of merit zT vs temperature for all the samples investigated.

Conclusions

We prepared a number of solid solution of the Zintl compounds $CaZn_2Sb_2$ and $CaMg_2Sb_2$ crystallizing in the $CaAl_2Si_2$ structure. The thermoelectric properties of Na-doped $CaMg_2Sb_2$ were investigated for the first time in this study. An effective mass analysis finds a step like function with regards to composition, indicating transport is changing from one set of bands to another roughly at the composition $CaMgZnSb_2$. We find the sample with composition $Ca_{.99}Na_{.01}ZnMgSb_2$ has the highest *zT* of 0.87 at 575 °C at optimum carrier concentration and due to the low lattice thermal conductivity reached. Herein, we also demonstrate how a Klemens type model taking into account disorder on the transition metal site can explain the lattice thermal conductivities of the alloyed compositions.

Conflicts of interest

There are no conflicts to declare.

Acknowledgements

This research was carried out under a contract with the National Aeronautics and Space Administration and was supported by the NASA Science Missions Directorate's Radioisotope Power Systems Technology Advancement Program. This work made use of the J.B.Cohen X-Ray Diffraction Facility supported by the MRSEC program of the National Science Foundation (DMR-1720139) at the Materials Research Center of Northwestern University and the Soft and Hybrid Nanotechnology Experimental (SHyNE) Resource (NSF ECCS-1542205.)

References

1. L.L.N.L., *Energy Enviroment Directorate*, 2016.
2. E. S. Toberer, A. F. May and G. J. Snyder, *Chemistry of Materials*, 2010, **22**, 624-634.
3. Z. Chen, Z. Jian, W. Li, Y. Chang, B. Ge, R. Hanus, J. Yang, Y. Chen, M. Huang, G. J. Snyder and Y. Pei, *Adv Mater*, 2017, **29**.
4. C. Fu, T. Zhu, Y. Pei, H. Xie, H. Wang, G. J. Snyder, Y. Liu, Y. Liu and X. Zhao, *Advanced Energy Materials*, 2014, **4**.
5. Y. Pei, X. Shi, A. LaLonde, H. Wang, L. Chen and G. J. Snyder, *Nature*, 2011, **473**, 66-69.
6. Y. Tang, Z. M. Gibbs, L. A. Agapito, G. Li, H. S. Kim, M. B. Nardelli, S. Curtarolo and G. J. Snyder, *Nat Mater*, 2015, **14**, 1223-1228.
7. H. Wang, Y. Pei, A. D. LaLonde and G. J. Snyder, in *Thermoelectric Nanomaterials*, Springer, 2013, pp. 3-32.
8. A. F. May and G. J. Snyder, *Thermoelect Energ*, 2012, K1-K18.
9. G. J. Snyder and E. S. Toberer, *Nat Mater*, 2008, **7**, 105-114.
10. S. Gorsse, P. B. Pereira, R. Decourt and E. Sellier, *Chemistry of Materials*, 2010, **22**, 988-993.
11. M. Schrade, K. Berland, S. N. H. Eliassen, M. N. Guzik, C. Echevarria-Bonet, M. H. Sorby, P. Jenus, B. C. Hauback, R. Tofan, A. E. Gunnaes, C. Persson, O. M. Lovvik and T. G. Finstad, *Sci Rep*, 2017, **7**, 13760.
12. H. Li, X. Su, X. Tang, Q. Zhang, C. Uher, G. J. Snyder and U. Aydemir, *Journal of Materiomics*, 2017, **3**, 273-279.
13. J. R. Watling and D. J. Paul, *J Appl Phys*, 2011, **110**.
14. J. Yang, G. P. Meisner and L. Chen, *Appl Phys Lett*, 2004, **85**, 1140-1142.
15. H. Wang, J. L. Wang, X. L. Cao and G. J. Snyder, *J Mater Chem A*, 2014, **2**, 3169-3174.
16. J. Shen, X. Zhang, S. Lin, J. Li, Z. Chen, W. Li and Y. Pei, *J Mater Chem A*, 2016, **4**, 15464-15470.
17. S. M. Kauzlarich, S. R. Brown and G. J. Snyder, *Dalton T*, 2007, DOI: 10.1039/b702266b, 2099-2107.
18. A. Zevalkink, E. S. Toberer, W. G. Zeier, E. Flage-Larsen and G. J. Snyder, *Energy Environ. Sci.*, 2011, **4**, 510-518.
19. S. Ohno, U. Aydemir, M. Amsler, J.-H. Pöhls, S. Chanakian, A. Zevalkink, M. A. White, S. K. Bux, C. Wolverton and G. J. Snyder, *Advanced Functional Materials*, 2017, **27**.
20. U. Aydemir, A. Zevalkink, A. Ormeci, Z. M. Gibbs, S. Bux and G. J. Snyder, *Chemistry of Materials*, 2015, **27**, 1622-1630.
21. S. Ohno, K. Imasato, S. Anand, H. Tamaki, S. D. Kang, P. Gorai, H. K. Sato, E. S. Toberer, T. Kanno and G. J. Snyder, *Joule*, 2017, DOI: 10.1016/j.joule.2017.11.005.
22. G. S. Pomrehn, A. Zevalkink, W. G. Zeier, A. van de Walle and G. J. Snyder, *Angew Chem Int Edit*, 2014, **53**, 3422-3426.
23. F. Gascoin, S. Ottensmann, D. Stark, S. M. Haïle and G. J. Snyder, *Advanced Functional Materials*, 2005, **15**, 1860-1864.
24. A. F. May, M. A. McGuire, D. J. Singh, J. Ma, O. Delaire, A. Huq, W. Cai and H. Wang, *Phys Rev B*, 2012, **85**.

25. D. Stark, G. J. Snyder, Ieee and Ieee, *The synthesis of CaZn2Sb2 and its thermoelectric properties*, Ieee, New York, 2002.
26. E. S. Toberer, A. F. May, B. C. Melot, E. Flage-Larsen and G. J. Snyder, *Dalton T*, 2010, **39**, 1046-1054.
27. A. Zevalkink, W. G. Zeier, E. Cheng, J. Snyder, J. P. Fleurial and S. Bux, *Chemistry of Materials*, 2014, **26**, 5710-5717.
28. K. Guo, Q.-G. Cao, X.-J. Feng, M.-B. Tang, H.-H. Chen, X. Guo, L. Chen, Y. Grin and J.-T. Zhao, *European Journal of Inorganic Chemistry*, 2011, **2011**, 4043-4048.
29. J. Shuai, H. Geng, Y. Lan, Z. Zhu, C. Wang, Z. Liu, J. Bao, C. W. Chu, J. Sui and Z. Ren, *Proc Natl Acad Sci U S A*, 2016, **113**, E4125-4132.
30. J. Shuai, Z. Liu, H. S. Kim, Y. Wang, J. Mao, R. He, J. Sui and Z. Ren, *J Mater Chem A*, 2016, **4**, 4312-4320.
31. J. Shuai, Y. Wang, H. S. Kim, Z. Liu, J. Sun, S. Chen, J. Sui and Z. Ren, *Acta Materialia*, 2015, **93**, 187-193.
32. L. Song, J. Zhang and B. B. Iversen, *J Mater Chem A*, 2017, **5**, 4932-4939.
33. J. K. Burdett and G. J. Miller, *Chemistry of Materials*, 1990, **2**, 12-26.
34. J. W. Zhang, L. R. Song, G. K. H. Madsen, K. F. F. Fischer, W. Q. Zhang, X. Shi and B. B. Iversen, *Nat Commun*, 2016, **7**.
35. Z. M. Gibbs, F. Ricci, G. Li, H. Zhu, K. Persson, G. Ceder, G. Hautier, A. Jain and G. J. Snyder, *npj Computational Materials*, 2017, **3**.
36. J. F. Sun and D. J. Singh, *J Mater Chem A*, 2017, **5**, 8499-8509.
37. Z. M. Gibbs, H. Kim, H. Wang, R. L. White, F. Drymiotis, M. Kaviany and G. Jeffrey Snyder, *Appl Phys Lett*, 2013, **103**.
38. S. D. Kang and G. J. Snyder, *arXiv:1710.06896*, 2017.
39. A. D. LaLonde, T. Ikeda and G. J. Snyder, *Review of Scientific Instruments*, 2011, **82**.
40. K. A. Borup, J. de Boor, H. Wang, F. Drymiotis, F. Gascoin, X. Shi, L. D. Chen, M. I. Fedorov, E. Muller, B. B. Iversena and G. J. Snyder, *Energ Environ Sci*, 2015, **8**, 423-435.
41. S. Iwanaga, E. S. Toberer, A. LaLonde and G. J. Snyder, *Review of Scientific Instruments*, 2011, **82**.
42. J. J. Kuo, S. D. Kang, K. Imasato, H. Tamaki, S. Ohno, T. Kanno and G. J. Snyder, *Energ Environ Sci*, 2018, DOI: 10.1039/c7ee03326e.
43. H.-S. Kim, N. A. Heinz, Z. M. Gibbs, Y. Tang, S. D. Kang and G. J. Snyder, *Materials Today*, 2017, **20**, 452-459.
44. B. Abeles, *Phys Rev*, 1963, **131**, 1906-&.
45. P. G. Klemens, *Phys Rev*, 1960, **119**, 507-509.
46. J. Callaway and H. C. Vonbaeyer, *Phys Rev*, 1960, **120**, 1149-1154.
47. P. G. Klemens, *P Phys Soc Lond A*, 1955, **68**, 1113-1128.